remote sensing

MDPI

Article

UAV-LiDAR Measurement of Vegetation Canopy Structure Parameters and Their Impact on Land–Air Exchange Simulation Based on Noah-MP Model

Guotong Wu [1], Yingchang You [1], Yibin Yang [2], Jiachen Cao [1], Yujie Bai [1], Shengjie Zhu [3], Liping Wu [1], Weiwen Wang [1], Ming Chang [1,*] and Xuemei Wang [1]

[1] Guangdong-Hongkong-Macau Joint Laboratory of Collaborative Innovation for Environmental Quality, Institute for Environmental and Climate Research, Jinan University, Guangzhou 511443, China; wgt@stu2020.jnu.edu.cn (G.W.); youyc.jnu@gmail.com (Y.Y.); jiachenc@stu2018.jnu.edu.cn (J.C.); baiyujie@stu2020.jnu.edu.cn (Y.B.); wlp@stu2020.jnu.edu.cn (L.W.); wwangeci@jnu.edu.cn (W.W.); eciwxm@jnu.edu.cn (X.W.)

[2] School of Computer Science and Engineering, South China University of Technology, Guangzhou 510006, China; mrrockyoung@163.com

[3] Department of Environmental Science, Guangdong Polytechnic of Environmental Protection Engineering, Foshan 528216, China; zhushj@mail3.sysu.edu.cn

* Correspondence: changming@email.jnu.edu.cn

Abstract: Land surface processes play a vital role in the exchange of momentum, energy, and mass between the land and the atmosphere. However, the current model simplifies the canopy structure using approximately three to six parameters, which makes the representation of canopy radiation and energy distribution uncertain to a large extent. To improve the simulation performance, more specific canopy structure parameters were retrieved by a UAV-LiDAR observation system and updated into the multiparameterization version of the Noah land surface model (Noah-MP) for a typical forest area. Compared with visible-light photogrammetry, LiDAR retrieved a more accurate vertical canopy structure, which had a significant impact on land–air exchange simulations. The LiDAR solution resulted in a 35.0∼48.0% reduction in the range of perturbations for temperature and another 27.8% reduction in the range of perturbations for moisture. This was due to the canopy structure affecting the radiation and heat fluxes of the forest, reducing their perturbation range by 7.5% to 30.1%. To reduce the bias of the land surface interaction simulation, it will be necessary to improve the method of retrieving the canopy morphological parameterization through UAV-LiDAR on a continued basis in the future.

Keywords: LiDAR; forest parameters; canopy structure; land surface modeling

Citation: Wu, G.; You, Y.; Yang, Y.; Cao, J.; Bai, Y.; Zhu, S.; Wu, L.; Wang, W.; Chang, M.; Wang, X. UAV-LiDAR Measurement of Vegetation Canopy Structure Parameters and Their Impact on Land–Air Exchange Simulation Based on Noah-MP Model. *Remote Sens.* **2022**, *14*, 2998. https://doi.org/10.3390/rs14132998

Academic Editors: Dengsheng Lu, Guijun Yang, Langning Huo, Xiujuan Chai and Xiaoli Zhang

Received: 25 April 2022
Accepted: 20 June 2022
Published: 23 June 2022

1. Introduction

The land surface plays an important role in the weather/climate/Earth system. Land surface processes not only regulate the exchange of energy and mass (i.e., water, carbon dioxide, and aerosols) between the land and the atmosphere [1] but also determine the proportions of net radiation and surface energy fluxes. Furthermore, the distribution ratio of the land surface has a direct impact on both the atmospheric water cycle and biogeochemical cycles, especially nitrogen and carbon fluxes [2]. However, there are various uncertainties in the simulation of land surface processes [3], which may result from the parameterization of turbulent and mesoscale fluxes under land surface non-uniformity conditions such as those resulting from the nonlinearity of land surface processes and non-uniformity of land surface characteristics [4]. In addition to regulating the land surface processes, the sub-grid topography in the model also contributes to the uncertainties in the simulation [5]. In addition, simulation of land surface processes can face even more uncertainties due to the simplified parameterization of biochemical processes (e.g., the carbon

cycle) and biological feedback mechanisms in the models. These factors limit the ability of models to describe not only various land surface processes for different land surface conditions (e.g., snow, soils, and hydrology) but also the interactions among different land surface conditions [6,7]. Therefore, an accurate characterization of the sub-bedding surface in models can significantly reduce the disparity between observations and simulations [8] and improve the cycle and interannual results of simulations [9]. For this reason, it is essential to improve the simulation performance by specifying the surface information in numerical models precisely [10].

In the current global land surface models, the effect of the three-dimensional (3D) canopy structure tends to be underestimated [11]. The canopy structure is a simple geometric shape characterized by several parameters of the land surface boundary. In contrast, forest geometry is an important controlling parameter related to forest short-wave radiative transfer, subsequent snow surface shading, and radiative energy exchange between the atmosphere and the canopy. It is challenging to account for these vegetation features at large spatial scales [12].

Among the traditional methods of forest-resource surveying, the manual ground survey is a mainstream method for the accurate expression of the canopy structure. However, it is practically difficult to obtain large-scale forest parameters through field investigation due to the involvement of cumbersome equipment and the lack of staff and time [13]. As science and technology advance constantly, large-scale forest-resource monitoring has been enabled by the application of remote sensing, geographic information systems, and global positioning systems technologies in the field of forestry. In addition, the ability to compile efficient and automated forest inventories across various regions is enabled by the collection of high-resolution data through remote sensing techniques with a relatively small number of sets of field sample plots [14]. Ecosystem monitoring has been improved by time series of remote sensing images captured from various satellite platforms such as Landsat, Sentinel, and the Moderate Resolution Imaging Spectroradiometer (MODIS). Vertical information and the internal structure of plants, on the other hand, are typically ignored or represented by simplistic geometric models in the relevant ecological studies [15]. Chang et al. [16] developed a fast yet affordable method to obtain vegetation canopy parameters using unmanned aerial vehicles (UAVs). However, this method is ineffective in retrieving accurate topographic information and the vertical structure across the forest area due to the low accuracy of vegetation structure attributes extracted from these passive optical images. The widespread application of active remote sensing is assisted by the recent progress made in forestry remote sensing, e.g., in forestry measurement and investigation. Active remote sensing can be regarded as a promising supplement to traditional methods of remote sensing. As an active remote sensing technology, LiDAR (light detection and ranging) has demonstrated its ability to collect georeferenced data in a fast and accurate way. It can penetrate the tree canopy to extract 3D structural information [17], which makes it advantageous for tree detection. In addition, LiDAR data show greater robustness to occlusions and shading than passive optical data [18], and therefore the technique has been extensively applied to obtain the canopy structure parameters across various forest regions [19,20]. The various LiDAR platforms can be classified into different categories by resolution and spatial range, such as ground-based LiDAR, backpack and mobile LiDAR, airborne LiDAR, and satellite-based LiDAR. Ground-based LiDAR scanners are often installed on permanent tripods to gather data in a walk-and-stop mode, which makes it laborious to align multi-scan LiDAR data [21–23]. Despite having the longest ranging capability of the satellite-based LiDAR systems, the centralized platform performs worst in terms of resolution. Due to the recent progress made in integrated navigation techniques and simultaneous positioning and mapping algorithms, more possibilities have been presented for mounting ground-based laser scanners on mobile platforms, to significantly improve the efficiency of data collection [24,25]. With the development of UAV low-altitude photography technology, the integration of UAV and LiDAR (UAV-LiDAR) has been demonstrated to be advantageous in assisting forest investigations [26]. Integrat-

ing positioning and inertial measurement technologies, UAV-LiDAR has the capacity to considerably improve the ranging capability. Meanwhile, due to advanced manufacturing techniques, UAV-LiDAR has become increasingly lightweight and compact, which makes it more affordable. In summary, LiDAR not only enhances the flexibility of large-scale investigations significantly but also reduces their cost [27].

In previous studies, reference has been made to the huge amount of point-cloud data obtained using these new methods of quantitative remote sensing and the ability of these methods to characterize the 3D canopy precisely [28–30]. To accurately simulate the 3D radiation distributions, both voxel-based transfer models and discrete anisotropic radiative transfer models have been developed, in order to integrate the vegetation structure information into the solar radiation model, the vegetation dynamics model, and the cross-scale biodiversity model. For instance, Regaieg et al. [31] applied the DART model to examine the impact of the 3D canopy structure on chlorophyll fluorescence brightness and the radiation income and expenditure in deciduous forests. Through a new-generation Earth system model named CliMA, Braghiere et al. [32] investigated how the canopy structure enhances hyperspectral radiative transfer and the characterization of solar-induced chlorophyll fluorescence. Using the CliMA Land (v0.1) model, Wang et al. [33] assessed stomatal models at the stand level in both deciduous angiosperm and evergreen gymnosperm forests. However, these 3D canopy structures are not directly available in stand-alone land surface process models, nor are they available in the inland surface process modules coupled to large-scale environmental models such as climate models and air-quality models. Despite the fact that some 3D models suitable for the study of small-scale settings with complex structures exist, it remains difficult to apply them on a large scale due to the need for substantial computational resources [34].

Therefore, the proposed method of using 3D remote sensing data to improve the land surface model (LSM) is worthy of in-depth research. It is imperative to establish connections with LiDAR observations through land surface models and the parameterization of the observed 3D vegetation-canopy structure. The goal of this study is to update the LSM with more specific canopy structure information. We designed a technique for LSM canopy structure parameter improvement by integrating UAV and LiDAR photogrammetry and using visible-light photogrammetry as a control experiment. We attempted to address the following questions. (i) How accurate is LiDAR in terms of canopy parameter characterization, compared to visible-light photogrammetry? (ii) In terms of simulations of land surface processes, how did our replacement accurate canopy structure parameter model compare to the default model? (iii) What were the reasons for the above-mentioned model simulation variations? What part of the canopy structure did these variances relate to?

2. Materials and Methods

2.1. Study Area

This research was conducted at the Dinghushan forest ecosystem research station (CN-DIN). This station, surrounded by coniferous and broad-leaved mixed forests, occupies the core area of the Dinghushan nature reserve located in Zhaoqing, Guangdong Province, China (Figure 1a). The topography of this region shows a downward trend from the southwest to the northeast, with an elevation difference close to 990 m. Almost all the mountains and hills in this region have steep slopes, making it difficult to perform field measurements manually. The forest communities of the CN-DIN show complexity and diversity in species and include gully rain forests, southern subtropical evergreen broad-leaved forests, montane evergreen broad-leaved forests, and montane evergreen scrubs. The main vegetation of the CN-DIN is Pinus massoniana (Figure 1b). These favorable ecological conditions facilitate the efforts made to retrieve the forest structure information via the UAV platform.

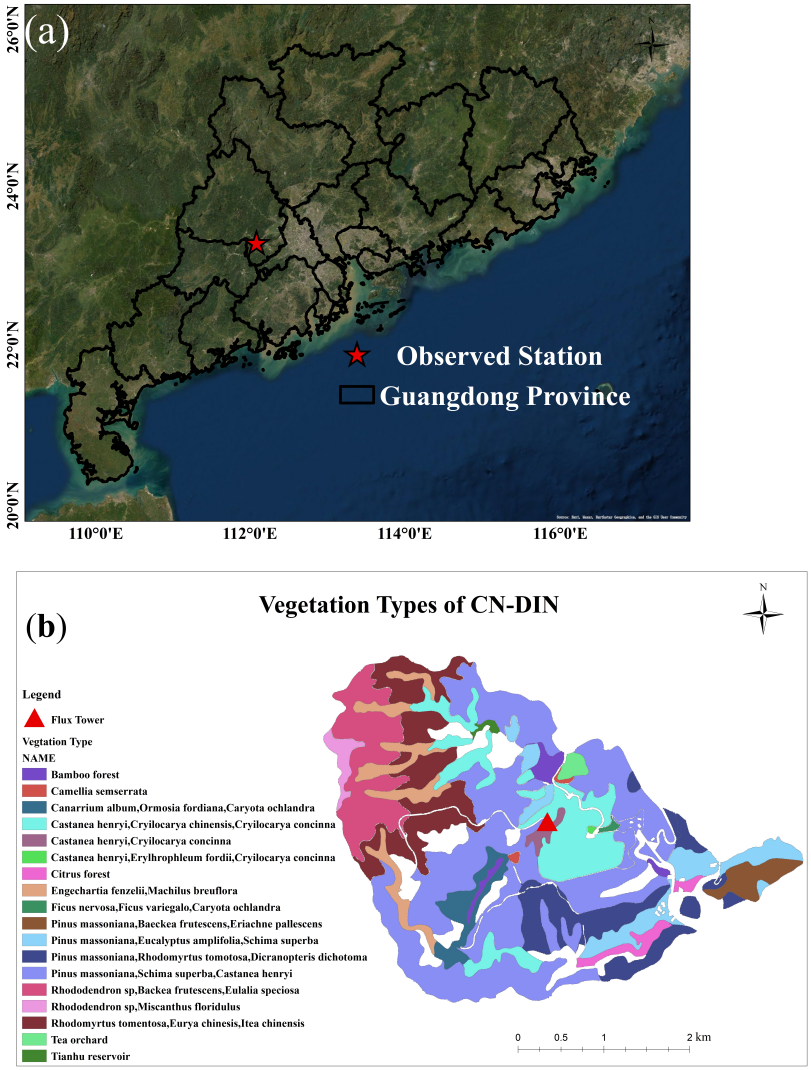

Figure 1. (**a**) Geographic location of the observed station. (**b**) Vegetation types at the CN-DIN.

2.2. Workflow

Figure 2 shows the general flowchart developed for factoring the canopy structure information into the model. By comparing the canopy parameters retrieved through these two different platforms, the different forest structures yielded by them were explored. Most of the programs were executed using automated tools and algorithms [35]. They were mainly divided into UAV-LiDAR data collection, point-cloud data processing, and acquisition of canopy parameters, together with canopy-parameter distribution functions driving land surface model calculations and model verifications.The image acquisition and data interpretation section is shown with a blue background, and the surface model simulation section is shown with an orange background.

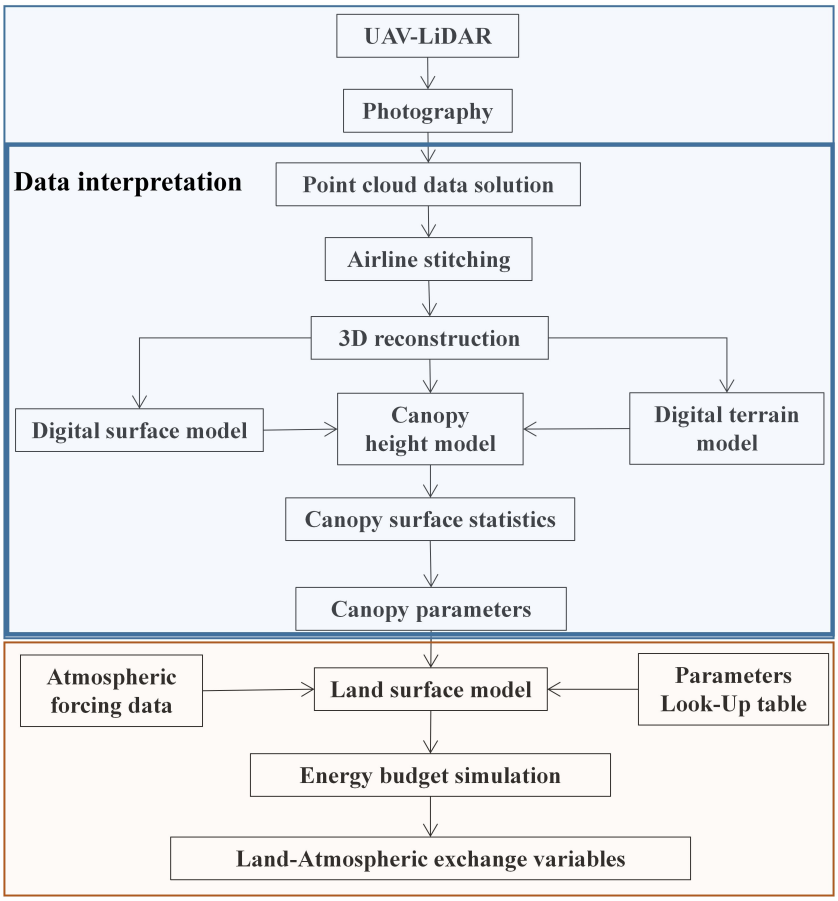

Figure 2. Flowchart for this study.

2.3. Image Acquisition and Data Interpretation

2.3.1. Photography

The experimental equipment included a DJI Matrice 600 Pro six-rotor UAV, used as the flight platform. Equipped with a LiAir V LiDAR system, it relies on the global navigation satellite system (GNSS) ground-based station to carry out system positioning. A DJI Phantom 3 Pro was used as a comparison flight platform, and the built-in visible-light camera was used to take photos.

Data collection was scheduled for 14 May 2021, with a collection coverage of about 0.0327 km^2. In this study, data collection was carried out using a LiDAR-equipped UAV, which flew along a preset course after being equipped with a GNSS ground base station. To ensure the comparability of the experiments, the LiDAR and the visible-light camera were configured with the same flight settings (flight height, flight speed, and flight trajectory) for retrieving the canopy structure parameters. The flight altitude was set as 100 m above the landing point, the flight speed was set to 4.3 m/s, and the average ground sample distance of the photos was fixed at 7.24 cm. The in-flight LiDAR and visible camera images had the same course overlap and side overlap settings of 80.0% and 75.0%, and the scanning angles were 37° and 70°, respectively. Figure 3a illustrates the flight trajectory of the UAV and the terrain height. Figure 3b presents three views of the spatial offset between the initial and calculated image positions, where the blue dots represent the initial image positions and the green dots indicate the calculated image positions. The offset between the initial ground-control point positions and their calculated positions is indicated by blue and green crosses, respectively. The dark green ellipse indicates the uncertainty of the absolute position for the beam block-leveling results. As can be seen clearly from the right panel, the accuracies of the images in the X, Y, and Z directions for the relative geographic location are 95.0, 100.0, and 100.0%, respectively.

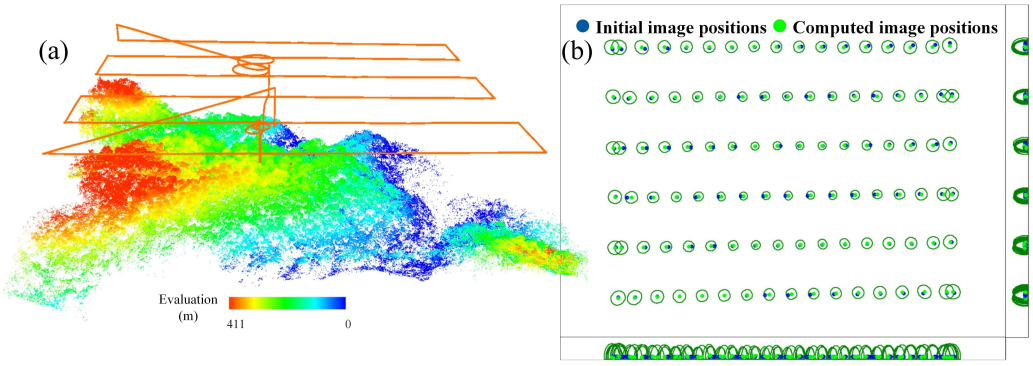

Figure 3. (**a**) Three-dimensional terrain display. The orange line shows the UAV flight trajectory. (**b**) Location uncertainty assessment map.

2.3.2. Data Interpretation

The method for processing the LiDAR and visible-light camera images to obtain the canopy 3D parameters was as follows. Firstly, the differential GPS data and IMU data collected during the aerial flight were decoded collectively to obtain the positioning and orientation data. In addition, the joint positioning and orientation data, the original point-cloud information, and the various parameters provided by the system were applied to solve the data to obtain the 3D coordinates of each laser point in the WGS-84 coordinate system. Then, the LiDAR data were correlated according to the overlapping area between the airstrip data. The only difference between these two experiments was in the point-cloud resolution software, which was LiGeoreference for LiDAR and Pix4Denterprise for the visible-light camera. Coarse difference detection and rejection processing were carried out in the course of preprocessing the data, due to the large number of coarse differences and systematic errors contained in the massive point-cloud dataset obtained by the airborne LiDAR system (i.e., the very high and very low points were rejected). The solved point-cloud densities in the two experiments were 153 points/m^2 and 325 points/m^2, respectively. They were both meeting the needs of interpolated range of digital elevation model data (CH/T 8024-2011).

Secondly, a progressive TIN densification filtering algorithm was used to distinguish the ground information from the laser point cloud. Moreover, a digital simulation of the ground topography was performed with limited topographic elevation data through inverse distance weighted interpolation (IDW) [36], i.e., using the digital elevation model (DEM) representing the bare ground surface (with vegetation and other features removed) and the digital surface model (DSM) representing the feature surface information [37]. Thirdly, the DSM was subtracted from the DEM to obtain a normalized point cloud, thus eliminating the effect of topographic relief on the elevation values of the point-cloud data, to construct the canopy height model (CHM). Furthermore, on the basis of the CHM, a single wood segmentation was performed using a watershed algorithm [38]. Finally, canopy structure parameters such as the single wood location, the height of trees, the canopy area, the diameter at breast height, the crown diameter, and the tree boundary were obtained through calculation and measurement of the single wood point cloud.

2.4. Land Surface Model Simulation

2.4.1. Atmospheric Forcing Data

The meteorological observations data included wind speed, wind direction, relative humidity, air temperature, pressure, downward short-wave radiation, and downward long-wave radiation, and these were collected from the CN-DIN from 1 January to 31 December 2019, with a temporal resolution of 30 min. Wind direction and speed, precipitation, and radiation were all observed from a 36 m height. The temperature, surface pressure, and relative humidity were measured at a height of 4 m. At a height of 27 m, where the near-

est observation layer to the tree canopy was located, both the sensible heat flux (SH) and the latent heat flux (LH) were collected using an open-path eddy covariance system termed CSAT3 (https://www.campbellsci.com/csat3 (accessed on 24 April 2022)) [39].

2.4.2. Land Surface Model Setup And Validation

The Noah-Multiparameterization (Noah-MP) land surface model was applied in this study to estimate the impact of the updated parameters. As a cutting-edge model, Noah-MP is applicable for describing the heat flow between the surface and the atmosphere by combining 12 biophysical and hydrological processes [39]. In the multilayer snow, permafrost, and aquifer models, these processes also take into account dynamic vegetation, stomatal conductivity, surface heat fluxes, water-vapor exchange coefficients, the radiative interactions between the vegetation canopy structure and the soil, the hydrological processes between the canopy and soil, and groundwater dynamics [40]. Furthermore, the results of the Noah-MP simulation can be improved by more accurate land surface heterogeneity and 3D plant structure parameterization for surface energy fluxes, soil moisture, and temperature [2]. Table 1 lists the parameterizations performed in this study. The underlying surface of the CN-DIN can be regarded as a mixed forest.

Table 1. The setup options of the Noah-MP land surface model.

Type of Land Surface Process	Physical Processes	Description	Options	Contents
Vegetation	OPT_DVEG	Mainly used to calculate leaf area index and vegetation cover.	2	Dynamic Vegatation Model [41]
	OPT_CRS	Calculation of foliar stomatal impedance. Stomatal impedance influences the magnitude of the latent heat flux brought about by vegetation through leaf transpiration.	1	Ball–Berry Scheme [42]
	OPT_SFC	The calculation of the SH transport coefficient C_h, which in the model reflects the strength of the energy exchange between land and air, is carried out.	2	Noah Type [43]
	OPT_RAD	Used to parametrically represent the canopy structure of the vegetation in the grid.	1	Gap = f (3D, cosz) [44]
Soil	OPT_BTR	For the calculation of soil moisture, which can influence stomatal conductivity, photosynthesis, and soil decomposition.	1	Noah Type [45]
	OPT_INF	Expresses the process of water infiltration in permafrost.	1	NY06 [46]
	OPT_TBOT	For the selection of boundary conditions of soil temperature.	2	Original Noah [47]
	OPT_STC	For the selection of snow/soil temperature time scenarios.	1	Semi-Implicit [40]
Water	OPT_RUN	Used to simulate runoff, groundwater, and the changes in soil moisture they cause.	1	SIMGM [48]
	OPT_FRZ	Used to calculate the amount of liquid and solid water in the soil when it freezes.	1	NY06 [46]
	OPT_ALB	Used to calculate the surface albedo of snow on the ground.	2	CLASS [49]
	OPT_SNF	Distinguishes between rainfall and snowfall.	1	Jordan [50]

To evaluate the accuracy of the simulation, the root mean square error (RMSE) and R-squared (R^2) were used to evaluate the simulated mean values for different heights of trees under the LPR and VPR scenarios (Equations (1) and (2)). The RMSE represents the magnitude of the modeling error between the simulated (SIM) and observed (OBS) values, and R^2 is used to evaluate the goodness of fit. A higher value of R^2, with a lower value of the RMSE, indicates that the simulation result is consistent with the observation result, and vice versa.

$$RMSE = \sqrt{\frac{1}{m}\sum_{i=1}^{m}(y_i - \hat{y}_i)^2} \quad (1)$$

$$R^2 = 1 - \frac{\sum_i (\hat{y}_i - y_i)^2}{\sum_i (\bar{y}_i - y_i)^2} \quad (2)$$

2.4.3. Vegetation Parameters Look-Up Table in Noah-MP

Noah-MP sets the main physical parameters that vary with vegetation type to drive the simulation of land surface processes. Table 2 illustrates the values of the parameters with high sensitivity when the dynamic vegetation scheme is used and the vegetation type is mixed forest [51]. LTOVRC controls carbon exchange from plants to the soil owing to leaf and stem senescence, whereas QE25 and VCMX25 directly control light-limited and export-limited photosynthesis, respectively (export limitation is regulated by local air pressure) [52]. SLA is used to calculate leaf and stem area indices and is dependent on plant type. The 3D vegetation model in the radiative transfer scheme employs HVT to determine the total available energy from the soil and plant surface, whereas Z0MVT regulates the surface advection potential.

Table 2. Noah-MP's vegetation-related parameters in mixed forest.

Parameter Name	Description	Value	Units
Z0MVT	Momentum roughness length	0.8	m
HVT	Height of canopy	16	m
RC	Tree crown radius	1.4	m
LTOVRC	Leaf and stem/organic turnover rate	0.5	s^{-1}
DILEFW	Coefficient for leaf stress death related to water	0.2	s^{-1}
RMF25	leaf maintenance respiration at 25 °C	3	μ mol m^{-2} s^{-1}
SLA	Single-side leaf area per kg	80	m^2 kg^{-1}
VCMX25	Maximum rate of carboxylation at 25 °C	55	μ mol m^{-2} s^{-1}
QE25	Quantum efficiency at 25 °C	0.06	μ mol m^{-2} s^{-1}

2.4.4. Energy Budget in Noah-MP

Land–atmosphere coupling is a complex process that is related to flux distribution, aerodynamic resistance, the resistance to endurance, and the soil moisture of the land–atmosphere system. The balance and distribution of radiation and energy are crucial for understanding the operation of terrestrial ecosystems and for the accuracy of climate change projections. The radiation balance of a forest is expressed as follows:

$$\begin{aligned} R_n &= USR - DSR + ULR - DLR \\ &= F_{veg}S_{av} + \left(1 - F_{veg}\right)S_{ab} + F_{veg}L_{av} + \left(1 - F_{veg}\right)L_{ab} \end{aligned} \quad (3)$$

$$F_{veg} = 1 - e^{-0.52 \times (LAI + SAI)} \quad (4)$$

The terms USR, DSR, ULR, and DLR represent upward short-wave radiation, downward short-wave radiation, upward long-wave radiation, and downward long-wave radiation, respectively, while R_n refers to the net radiation. The net short-wave radiation of vegetation and the net short-wave radiation of bare ground are denoted S_{av} and S_{ab}, respectively. L_{av} and L_{ab} represent the net long-wave radiation of vegetation and the net long-wave radiation of bare land. The vegetation fraction (F_{veg}) was calculated using the leaf area index (LAI) and stem area index (SAI).

The forest energy balance can be calculated by the following equation:

$$R_n = SH + LH + G + \varepsilon \cong SH + LH \quad (5)$$

The sensible heat flux is represented by SH, the latent heat flux is denoted LH, and the ground heat flux is indicated by G. In addition, ε stands for the residual term, which includes heat storage, photosynthetic energy consumption, etc. G and ε can be discounted as approximations in dense forest areas because they account for less than 5.0% of the total heat flux.

The equations for the heat fluxes over various surfaces are:

$$SH_{g,b} = \frac{\rho c_p \left(T_{g,b} - T_a\right)}{r_{ah}} \tag{6}$$

$$SH_{g,v} = \frac{\rho c_p \left(T_{g,v} - T_{ac}\right)}{r_{ah,g}} \tag{7}$$

$$SH_v = 2(L_e + S_e)\rho c_p (T_v - T_{ac})/r_{ab} \tag{8}$$

$$LH_{g,b} = \rho c_p \left(e_{g,b} - e_a\right)/\gamma(r_{ah} + r_{soil}) \tag{9}$$

$$LH_{g,v} = \frac{\rho c_p \left(e_{g,v} - e_{ac}\right)}{\gamma\left(r_{ah,g} + r_{soil}\right)} \tag{10}$$

$$LH_v = \rho c_p (e_v - e_{ac})\gamma(C_e^w + C_t^w) \tag{11}$$

In the above equations, $SH_{g,b}$ ($LH_{g,b}$) is the SH (evaporation flux from the bare ground), $SH_{g,v}$ ($LH_{g,v}$) is the SH from the vegetated ground (vegetated canopy evaporation heat flux from intercepted precipitation), and SH_v (LH_v) is the SH from the vegetation canopy (transpiration heat flux from the vegetation canopy). In addition, ρ represents the psychometric constant. T_a (e_a), T_{ac} (e_{ac}), T_v (e_v), $T_{g,v}$ ($e_{g,v}$), and $T_{g,b}$ ($e_{g,b}$) refer to the air, canopy air, vegetation canopy surface, vegetated ground surface, and bare ground temperatures (surface water vapor pressure), respectively. The heat resistance coefficients. denoted r_{ah} and $r_{ah,g}$, are linked to the surface layer turbulent transfer heat coefficient at the reference height and below the canopy, respectively. The leaf boundary layer resistance per unit leaf is indicated by r_b, and the wet leaf conductance is represented by C_e^w. The dry leaf stomatal conductance, denoted C_t^w, is associated with the photosynthetic rates given in the carbon budget.

3. Results

3.1. Characteristics of Measurement Results

In this study, the mean values and error ranges of six canopy structure parameters of LiDAR photographic measurements (LPR) and visible photographic measurements (VPR) were obtained by processing the photographic results to investigate the differences in canopy structure revealed by LiDAR and visible photography (Table 3). For the CN-DIN region, the values of averaged tree height, averaged canopy radius, and leaf area index (LAI) retrieved by the LPR were 16.35 m, 7.84 m, and 4.28, respectively. The VPR retrieved averaged tree height, averaged canopy radius, and leaf area index (LAI) values of 16.00 m, 9.61 m, and 0.48, respectively.

Table 3. Average values of the canopy structure.

Contents	LPR	VPR	Observed (References)
Average tree height (m)	16.35 ± 2.19	16.02 ± 7.07	7.0∼16.7 [53]
Tree diameter at breast height (cm)	2.22 ± 1.95	1.48 ± 1.60	5.1∼21.9 [54]
Canopy diameter (m)	7.84 ± 1.78	9.61 ± 2.35	3.0∼16.0 [55]
Leaf area index	4.28 ± 2.38	0.48 ± 0.43	6.5 ± 0.7 [56]
Canopy cover	0.81 ± 0.18	0.48 ± 0.32	>0.8 [57]
Gap fraction	0.19 ± 0.18	0.52 ± 0.42	0.1∼0.2 [58]

Although the LPR and VPR simulations were closer in terms of tree height, the disparities in the computation of other canopy structure factors were still significant. In the same region, the LPR's DBH (diameter at breast height) increased by 0.74 cm, but the RC (crown radius) decreased by 1.77 m. The three indices LAI, canopy cover, and gap percentage had the most significant variances, ranging from 39.5% to 88.8%. Except for DBH and LAI, the LPR had a small margin of error, and it exhibited 219.0%, 32.0%, 77.8%, and 133.3% decreases in average tree height, RC, canopy cover, and gap fraction, respectively.

To investigate the accuracy of the data obtained by LPR and VPR, the mean of the results obtained by these two methods was compared with field measurements (observed values) from other studies. The mean tree height values for LPR and VPR were determined to be the closest to the upper-limit value of the field measurements. In the sample plots, the mean values of both LPR and VPR RC were within the tree shape interval of the dominant tree species. Plant canopy height and silhouette shape can be accurately captured using both LiDAR and visible photography. The results of the statistics and calculations retrieved by LPR are comparable to the DBH results for mixed forests in the Dinghushan sample site. By generating laser pulses and receiving echoes to produce a high-density data point cloud, LPR can acquire a more accurate canopy structure. The LPR LAI, canopy cover, and gap fraction were all closer to the observed LAI of mixed forests than the VPR LAI. This may be attributed to the fact that passive optical imagery used for visible-light photogrammetry, which depends on the observed surface reflectance, encounters significant limitations when linked to vegetation [15]. Consequently, a small number of solved point clouds and significant errors were present in the LAI representation, vegetation cover, etc.

To further compare the acquisition of canopy structure parameters in the area using LiDAR and visible-light images, the distributions for HVT (vegetation top height), DBH (tree diameter at breast height), and RC (canopy radius) were obtained by solving for the LPR and VPR, and their fits were calculated (Figure 4). The HVT, DBH, and RC values of the LPR solution exhibited GaussAmp, Allometric 1, and lognormal distributions, with R^2 values of 0.80, 0.75, and 0.85, respectively. The HVT, DBH, and RC of the VPR solution exhibited GaussAmp, Allometric 1, and GaussAmp distributions, with R^2 values reaching 0.86, 0.99, and 0.95, respectively. As shown in Figure 4, the percentage of trees with DBH in the interval 1.0–4.9 m was 83.1%, while it was 52.0% for the LPR and VPR in 2021, respectively. In addition, it was 2.7% and 2.4%, respectively, for the 5.0–9.9 m interval. The LPR and VPR results obtained in this study were found to be consistent with the tree population curves sourced from the field survey of Dinghushan conducted by Li et al. [59] in October 2020. A total of 83.0% of the trees were measured to be in the DBH range of 1.0–4.9 m, and 11.2% were in the range of 5.0–9.9 m. LPR showed a distribution that was more consistent with the field observations. Unlike LiDAR, visible-light photography was incapable of accurately capturing the vertical structure of the forest.

The input parameters of the Noah-MP model were adjusted based on the above measurement results and fitting functions. Figure 5 shows the relationship between RC and HVT obtained from LiDAR (i.e., LPR) and visible light (i.e., VPR). The tree height used in LPR was the top vegetation height obtained from LiDAR (i.e., HVT from LPR), and the tree height used in VPR was the top vegetation height obtained from the visible-light camera (i.e., HVT from VPR). Under different scenarios, RC was replaced with the equations corresponding to HVT (Figure 5), which were entered into Noah-MP instead of the default values of the model (Table 4).

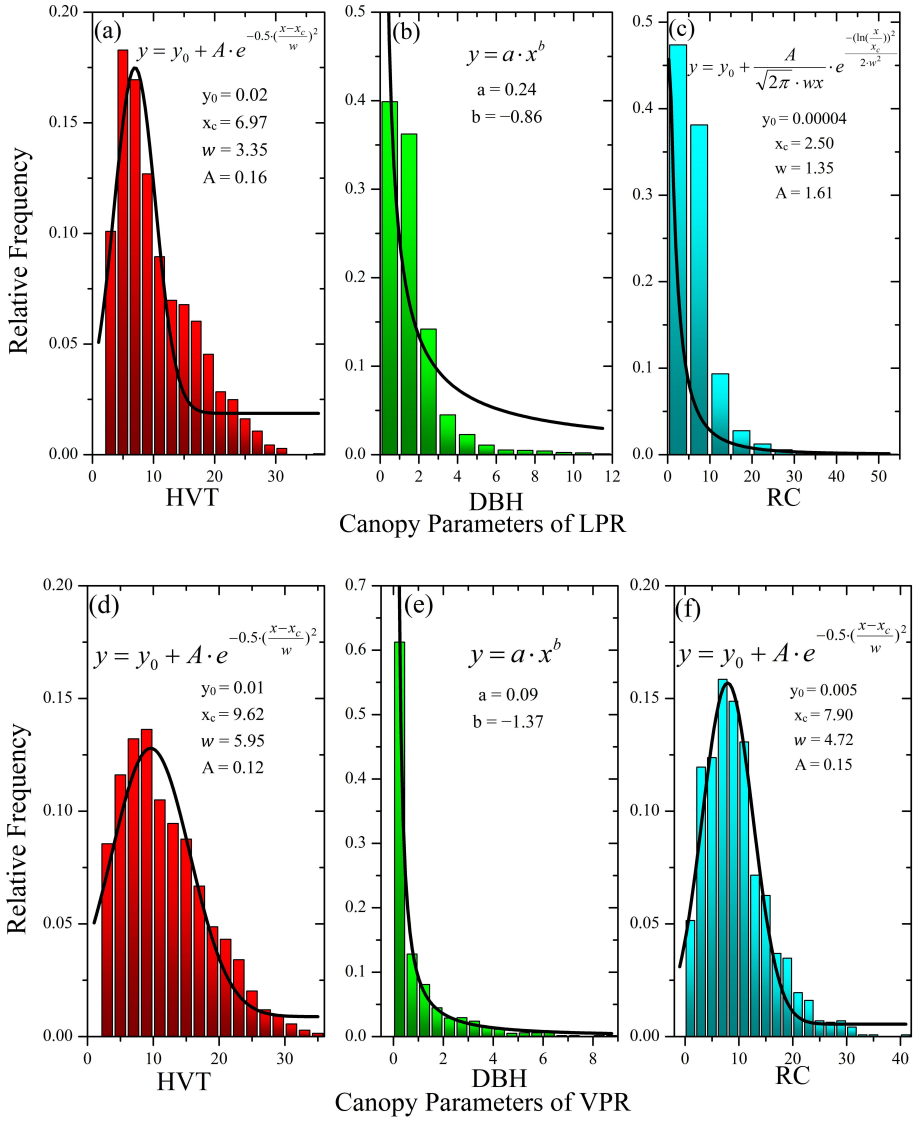

Figure 4. Histograms of the distributions of canopy parameters obtained from LPR (**a**–**c**) and VPR (**d**–**f**). Black curves are fits to the canopy parameter distributions.

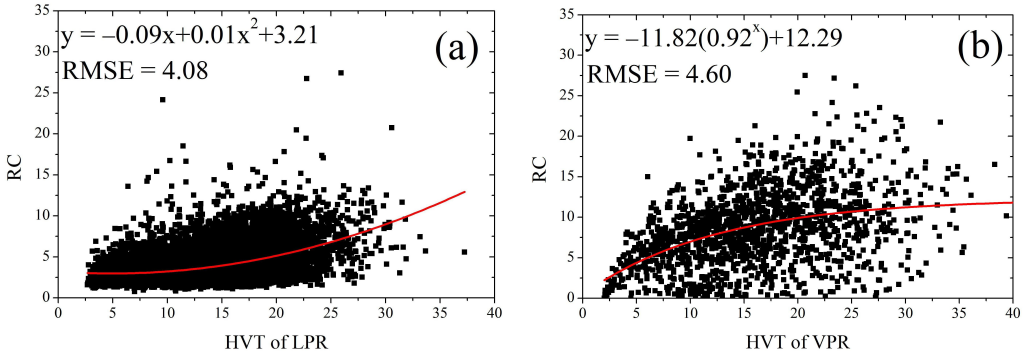

Figure 5. Relationship between HVT and RC driven by LPR (**a**) and VPR (**b**). Red lines indicate linear fits.

Table 4. HVT and RC functions for Noah-MP inputs.

Variables	Default	LPR	VPR
HVT	16.0	HVT from LPR	HVT from VPR
RC	1.4	$-0.09 \times \mathrm{HVT} + 0.01 \times \mathrm{HVT}^2 + 3.21$	$-11.82 \times 0.92^{\mathrm{HVT}} + 12.29$

3.2. Results of the Simulated Canopy Temperature and Humidity Profiles

As for the assessment of plant carbon absorption processes within the land surface model, the model can be better constrained and improved with more precise canopy parameter inputs. Temperature, soil moisture, and vegetation growth characteristics may all be affected by these findings [60]. To fully understand the impact of accurate canopy parameter inputs on these changes, the simulation results related to temperature were extracted for comparison. Figure 6 shows the box plots of vegetation temperature (Tv), canopy air temperature (Tac), ground temperature (Tg), soil temperature (Ts), and soil moisture (SMC), averaged for different tree heights. The surface 0.1 m and 1.0 m under the ground were treated as the first and second soil layers, respectively. As shown in Figure 6, the mean values of the LPR scenario for Tv, Tac, Tg, Ts_1, and Ts_2 were 296.0 ± 0.13 K, 295.7 ± 0.11 K, 296.0 ± 0.14 K, 296.0 ± 0.13 K, and 296.1 ± 0.12 K, respectively. The mean values of the VPR scenario for Tv, Tac, Tg, Ts_1, and Ts_1 were 295.9 ± 0.22 K, 295.6 ± 0.17 K, 295.9 ± 0.25 K, 296.1 ± 0.24 K, and 296.2 ± 0.23 K, respectively. The CN-DIN temperature profile observations were represented by the temperatures at 15 m, at 9 m, the surface air temperature, 0.1 m below ground, and 1 m below the ground, and these were 294.4 K, 294.3 K, 294.5 K, 294.6 K, and 294.8 K. According to the above simulation, there was an overestimation of 5.7–6.8% and 5.9–6.5% of the observed temperature by LPR and VPR, respectively, with relatively insignificant deviations, and the outcome of the simulation using the Noah-MP model was satisfactory. The LPR scenario had 3 to 22 times more temperature outliers than the VPR scenario, for which the perturbation range of temperature was reduced by 35∼48%. The observed soil moisture values were obtained as 0.247 m^3/m^3 and 0.258 m^3/m^3. The LPR and VPR simulation for SMC_1 and SMC_2 was 0.231 m^3/m^3, 0.230 m^3/m^3, 0.230 m^3/m^3, and 0.229 m^3/m^3, respectively, representing underestimations of 6.9%, 12.2%, 7.4%, and 12.7%, respectively. The simulation results for soil moisture were more comparable to the observation values than under the LPR scenario, and the margin of error in the simulations was reduced by 27.8%.

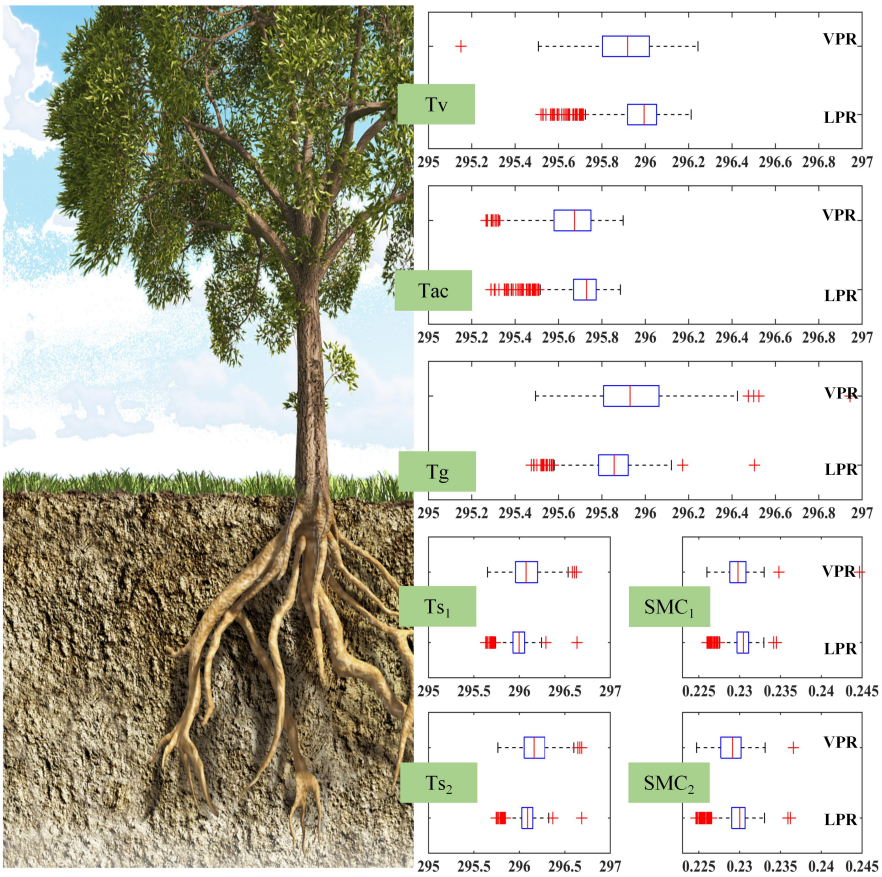

Figure 6. Diagrams for simulated vegetation temperature (Tv), canopy air temperature (Tac), ground temperature (Tg), soil temperature (Ts), and soil moisture (SMC). Red lines indicate the median, the bottom and top edges of the boxes indicate the 25th and 75th percentiles, and red crosses indicate outliers.

4. Discussion

4.1. Diagnosis of the Upward Radiation Simulation

Firstly, the simulation difference for temperature in the canopy was identified from the difference in the capacity of radiation acceptance. Driven by the same downward radiation, the upward radiation simulation differed due to different canopy characterizations. The characterization of the canopy structure had an immediate impact on the distribution of solar radiation in the canopy. However, the multilayered character of canopies was not well represented in earlier models. To explore the effect of different multilayered characteristics of the tree canopy on the radiation distribution, two different tree height parameters were set to drive the model, with different simulated *USR* and *ULR* values used for comparison (Figure 7). The radiation process was largely affected by vegetation and ground temperature [61]. The RAD process of the model had an immediate impact on both the short-wave radiation absorbed by the vegetation and the photosynthetically active radiation (PAR). In this study, OPT_RAD = 1 was chosen, which is based on the assumption that the gap probability is a function of the solar zenith angle and the 3D structure of the vegetation canopy and that short-wave radiation is intercepted by the canopy. The simulated *USR* under the default, LPR, and VPR scenarios was underestimated by an average of approximately 2.6, 3.3, and 2.8 W/m^2 throughout the year, compared to the observed values. In addition, the simulated *ULR* was overestimated by 11.3, 6.7, and 6.8 W/m^2. The *USR* and *ULR* simulated under the two improved scenarios were more accurate in the same range of tree heights relative to the default case of the model. The difference between the *USR*

and observed values from the simulations under the LPR and VPR scenarios ranged from 31.7% to 60.6%, with the range of perturbation reduced in the LPR scenario by 30.1% compared to VPR. The difference between the *ULR* and observed values ranged from 0.8% to 2.2%, with the range of perturbation reduced in the LPR scenario by 13.6% compared to VPR. This is suspected to result from the correct solution of the LPR and VPR scenarios for the vegetation canopy diameter. There was less pore space available between the canopy for short-wave transition, the canopy shading of its substratum and the land below increased, and the vegetation absorbed more short-wave radiation, light, and effective radiation, resulting in a higher Tv. Accordingly, with less short-wave radiation absorbed by the ground through the canopy, more long-wave radiation was reflected, leading to a reduction in Tg and Ts. For the same tree height, the *USR* and *ULR* of the VPR simulations became more accurate due to a more significant RC improvement for the VPR forest canopy. As a result, there was a lower underestimation of *USR* and a higher overestimation of *ULR* in the LPR scenario. However, with an increase in tree height and canopy width, the vegetation gap in the VPR simulation became too small to absorb much short-wave radiation and PAR when HVT exceeded 30 m. The accuracy of the simulated *USR* and *ULR* decreased by 9.5% and 3.6% relative to LPR, while the range of perturbations was widened significantly for the VPR simulation.

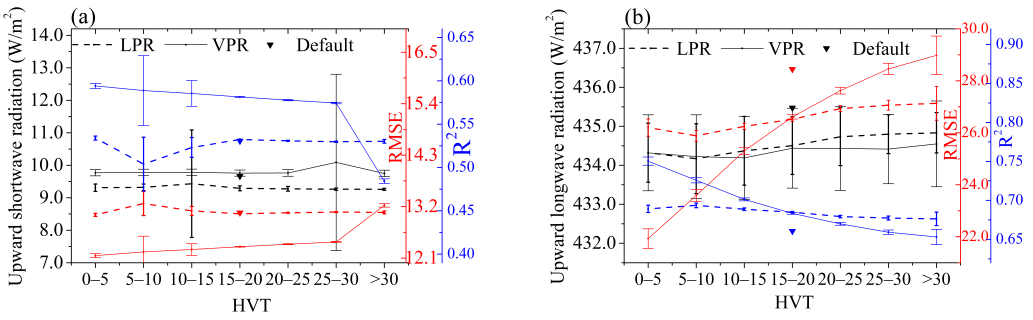

Figure 7. Accuracy assessment of radiation simulations for different scenarios. (**a**) Upward short-wave radiation and (**b**) upward long-wave radiation. Black lines represent values, red lines represent RMSE, and blue lines represent R^2. Vertical bars represent the standard deviations of the data.

4.2. Diagnosis of the Surface Heat Flux Simulation

It was revealed that the temperature simulations varied, which is attributed to *LH* and *SH* effects. According to Noah-MP's OPT_SFC process, *SH* was the direct variable that affected the temperature differential between the ground and the heat exchange coefficient. The discrepancies in Ts and Tv resulted from the variations in turbulent exchange coefficients simulated in the SFC process, which also causes the *SH* differences (Equations (6)–(8)). While ground exchange coefficients were related to tree height, differences in the canopy structure can affect the accuracy of latent heat processes in the forest, which not only leads to variations in the distribution of surface energy but also affects *SH* and *LH* exchange between the ground and the atmosphere. Therefore, the differences in *SH* and *LH* obtained under the LPR and VPR scenarios were explored. Figure 8 shows the accuracy of the surface energy simulated for different canopy heights in the CN-DIN region. The annual mean values of *SH* and *LH* were observed to be 32.59 W/m^2 and 21.04 W/m^2, respectively. Upon comparison between the simulated and observed values, a significant difference (overestimation) was found in *SH*. In addition, a slight difference was found between the simulated *LH* and the observed *LH* (underestimation), which may result from the excessively strong coupling of the Noah-MP model that led to the transfer of excess energy and water vapor [62,63]. In contrast, the *LH* values were significantly affected by the level of water availability and the exchange coefficient, with a narrow range of variation.

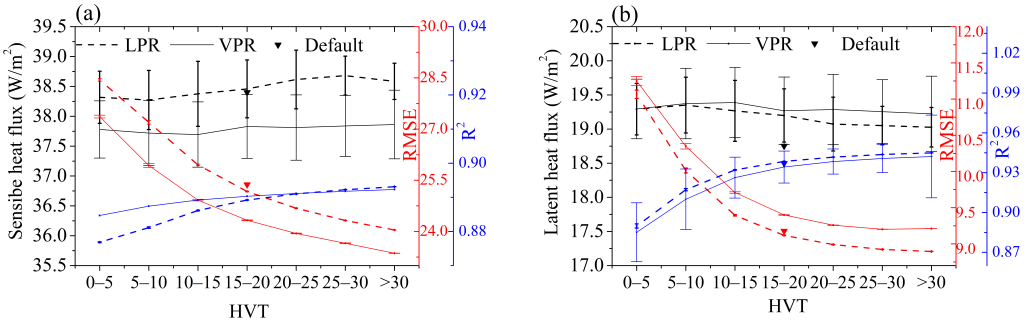

Figure 8. Accuracy assessment of energy simulations under different scenarios. (**a**) Sensible heat flux and (**b**) latent heat flux. Black lines represent values, red lines indicate RMSE, and blue lines refer to R^2. Vertical bars represent the standard deviations of the data.

In this study, the approximate range of *SH* differences obtained between the LPR and VPR scenarios was from 11.4% to 17.7%, with a 10.9% reduction in the range of perturbations compared to VPR under the LPR scenario. This is likely to be the main contributor to the difference in the temperature simulations. As a key parameter for the transfer of energy from the surface to the lower atmosphere, the surface exchange coefficient C_h indicates the strength of ground–air coupling. In contrast, LiDAR data enable the detailed 3D measurement of the forest structure [64], making more accurate height estimates achievable for low shrubs and tall trees in the forest. In this study, the strength of the ground–air coupling could be more accurately characterized under the LPR scenario, with a narrow range of perturbations in *SH* and minor temperature perturbations.

The approximate range of *LH* differences as obtained from the simulations of the LPR and VPR scenarios was from 2.9% to 7.4%, with a 7.5% reduction in the range of perturbations compared to VPR under the LPR scenario. In this study, the simulated differences in *LH* were found to be more significant, compared to the results obtained by Chen et al. [65] from woodland. This is attributable to the overestimation of *SH* for a constant $C_{zil} = 0$ (C_{zil} is an empirical coefficient related to the roughness length of moisture and heat). With more heat transferred from the surface to the atmosphere at greater C_h, the skin temperature was reduced. The evaporation from the ground and canopy was slowed down by the declining skin temperature, making the underestimation more significant. In this case, a better performance was produced under the LPR scenario than in the VPR simulation, with a 3.5% decrease in the RMSE. This is because the differences in Tv, Tg, and F_{veg} had a combined effect on the differences in some of the *LH* components associated with canopy transpiration and ground evaporation, and ultimately on the total *LH* level. Therefore, this study focused on three *LH* components to better understand the causes of *LH* disturbance. As shown in Figure 9, the reductions in disturbance for LPR under the VPR scenario were $LH_{g,v}$ (i.e., 1.0 W/m^2), $LH_{g,b}$ (i.e., 0.2 W/m^2), and LH_v (i.e., 2.3 W/m^2), respectively. Compared to VPR, the three *LH* components of LPR were less perturbed but more accurately simulated for the same tree height range. The rise in Tv of LPR (Figure 6) lowered the absorption rates, reduced the leaf area index, increased the stomatal resistance, and thus suppressed transpiration. Despite a smaller F_{veg} and a larger bare ground area simulated under the LPR scenario, the overall effect of less significant radiation uptake by the soil and lower soil temperatures was mitigated by soil evapotranspiration. Therefore, a smaller overall *LH* was simulated under the LPR scenario compared to the VPR scenario. The level of LPR soil moisture was higher than for VPR, thus resulting in a narrower range of moisture simulation perturbations than for VPR.

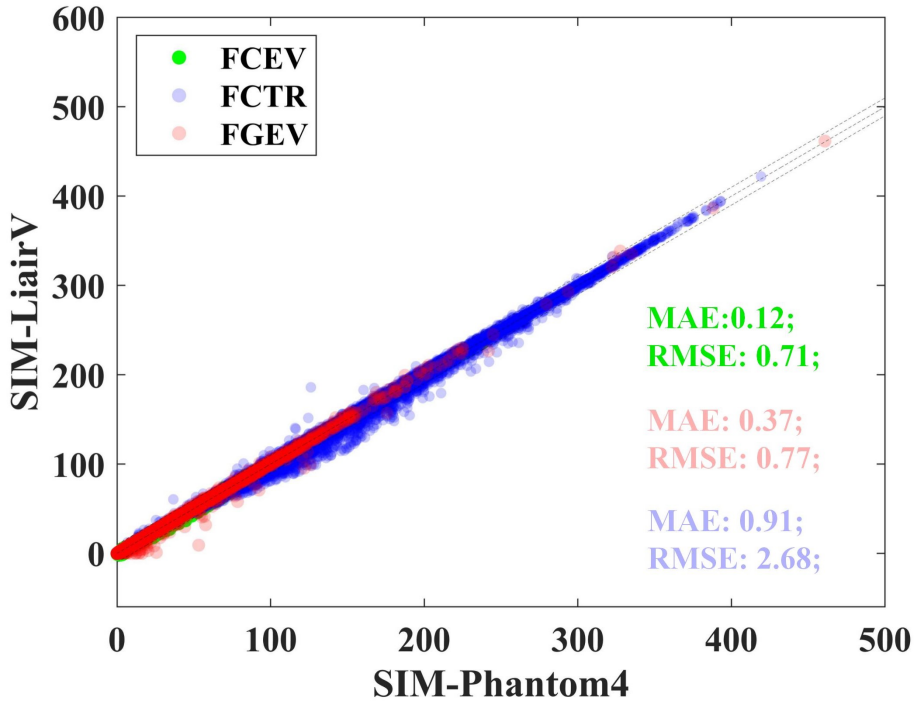

Figure 9. Comparison of the *LH* components under the LPR and VPR scenarios. The green font represents $LH_{g,v}$, the pink font represents $LH_{g,b}$, and the blue font represents LH_v.

4.3. Limitations and Possible Improvements

The approach proposed in this study is an initial attempt to associate the canopy structure obtained by UAV-LiDAR with a simple scenario of the LSM. In some cases, there was significant uncertainty in performance for the parameters of the input models used in this study. Therefore, the focus of future research will be to establish how to better propagate its large estimation uncertainty for constraining the LSM. Furthermore, our study failed to reflect the seasonal changes in the canopy structure in the offline simulation configuration of Noah-MP. The changes in the roughness length of momentum occurred through the seasonal changes in the proportion of green vegetation, and the seasonal changes in vegetation fraction affected the ratio of heat to the roughness length of momentum. Future research based on LiDAR-observed plant canopies and cover data over time might result in more valuable and objective advances in the land–air coupling. Nonetheless, our study demonstrated that the optimal vegetation canopy structure can enhance temperature and moisture modeling, especially through the improved modeling of latent heat fluxes. These findings provide a reference for those scientists interested in future modeling studies of surface reactions to the atmosphere and climate system. Therefore, it is necessary to continue enhancing the parametric description of the canopy morphology based on the results of this experiment, thus improving the accuracy of simulated near-surface land surface processes and canopy dynamics.

Although current LiDAR technology is unmanned and miniaturized, its overall cost of usage is high, due to the costly laser-detecting equipment, restricting LiDAR technology's wider deployment. As a result, it is necessary to find an alternative technology that can balance economic considerations with high spatial resolution. By comparing the canopy structures and model input data obtained by the two methods of photography, this study used visible drone photography as a control test that was one third as expensive or less than airborne LiDAR technology [66], to verify whether visible drone photography results can be used as a complement to LiDAR for larger areas or longer data acquisition times. In the study, HVT was discovered to be the most sensitive parameter in the model. The correlation coefficient between the two approaches was found to be quite high when comparing the tree height of the canopy point-cloud model derived by LPR and VPR

methods. As a result, this study anticipates that in the future, LiDAR could be used to obtain high-precision terrain or calibration data for areas with low terrain variation, and then photogrammetry can be used to conduct multi-period aerial surveys to obtain vegetation canopy height information in different seasons, resulting in low-cost long-series, multi-period observations. This would allow for more precise ground monitoring findings, which could help with decision-making at a local or regional scale [67].

5. Conclusions

Herein, a new method was developed to retrieve canopy parameters by means of UAV-LiDAR photogrammetry. The new method was capable of capturing the forest-canopy structure with centimeter accuracy and high cost-effectiveness. This new method retrieved an accurate forest canopy over a typical subtropical forest area of the Dinghushan forest ecosystem research station (CN-DIN). The canopy structure parameters retrieved by UAV-LiDAR were updated in the Noah-MP model to improve the performance of the numerical simulation.

According to the research results, the method was effective in capturing more detailed forest canopy characteristics such as tree height, the diameter at breast height, and the canopy radius, in the CN-DIN area. The aforementioned forest canopy characteristics exhibited GaussAmp, Allometric 1, and lognormal distributions, respectively. The mean values were 16.35 m, 7.84 m, and 4.28 for the tree height, canopy diameter, and leaf area index retrieved from LiDAR, respectively.

Regarding the effect of different canopy heights on the simulation of temperature and moisture, the updating of these local canopy parameters had a more significant impact on the simulation of temperature. The LiDAR photogrammetry results (LPR) scenario simulated vegetation and canopy air, ground, and soil temperatures, with errors from 5.7% to 6.8% compared with the results of observations. Compared to the visible-light photogrammetry results (VPR) scenario, the LPR scenario showed a 35.0∼48.0% reduction in the range of perturbations for temperature and a 27.8% reduction in the range of perturbations for moisture.These results indicate that the accurate canopy parameters retrieved from LiDAR can help to improve the model simulation. The accurate representation of the canopy structure by LPR allowed for a more detailed description of the short-wave radiation absorbed by the ground and the long-wave radiation reflected by the canopy, as well as the processes of sensible and latent heat fluxes, by influencing the surface exchange coefficient C_h and the strength of the ground–air coupling. Ultimately, temperature and moisture were affected. The LPR simulations of the forest upward short-wave radiation and long-wave radiation were reduced by 30.1% and 13.6% in the range of disturbance, compared to the VPR scenario. The LPR simulations of sensible and latent heat fluxes were 10.9% and 7.5% less perturbed than in the VPR scenario. Although there are disadvantages such as high cost and complex operation, LiDAR could be regarded as an important supplement to active remote sensing in the future, due to the high-precision retrieval of data.

Author Contributions: Conceptualization: M.C. and G.W.; methodology: M.C. and G.W.; software: J.C., S.Z., G.W. and Y.Y. (Yingchang You); formal analysis: G.W., Y.Y. (Yingchang You), Y.Y. (Yibin Yang), Y.B. and L.W.; supervision: M.C., W.W. and X.W.; validation: G.W.; visualization: G.W., Y.Y. (Yibin Yang); writing—original draft: G.W., Y.Y. (Yingchang You) and M.C. All authors have read and agreed to the published version of the manuscript.

Funding: This research was funded by National Natural Science Foundation under grant numbers 41705123, 42121004, and 41875010, the National Key Research and Development Plan under grant number 2017YFC0210103, the Special Fund Project for Science and Technology Innovation Strategy of Guangdong Province under grant number 2019B121205004, and the Guangdong Innovative and Entrepreneurial Research Team Program under grant number 2016ZT06N263.

Data Availability Statement: The data presented in this study are openly available in [FigShare] at [http://dx.doi.org/10.6084/m9.figshare.20124131].

Acknowledgments: This work was supported by the Research Team on Atmospheric Environmental Roles and Effects of Carbonaceous Species, Dinghushan Forest Ecosystem Research Station, Chinese Academy of Sciences, and by the High Performance Public Computing Service Platform of Jinan University.

Conflicts of Interest: The authors declare no conflict of interest.

Abbreviations

The following abbreviations are used in this manuscript:

USR	Upward short-wave radiation
ULR	Upward long-wave radiation
SH	Sensible heat flux
LH	Latent heat flux
LPR	LiDAR photogrammetry results
VPR	Visible-light photogrammetry results
Tv	Vegetation temperature
Tac	Canopy air temperature
Tg	Ground temperature
Ts	Soil temperature
SMC	Soil moisture

References

1. Fang, Y.; Zou, X.; Lie, Z.; Xue, L. Variation in Organ Biomass with Changing Climate and Forest Characteristics across Chinese Forests. *Forests* **2018**, *9*, 521. [CrossRef]
2. Pilotto, I.L.; Rodríguez, D.A.; Tomasella, J.; Sampaio, G.; Chou, S.C. Comparisons of the Noah-MP land surface model simulations with measurements of forest and crop sites in Amazonia. *Meteorol. Atmos. Phys.* **2015**, *127*, 711–723. [CrossRef]
3. Zhang, X.; Chen, L.; Ma, Z.; Gao, Y. Assessment of surface exchange coefficients in the Noah-MP land surface model for different land-cover types in China. *Int. J. Climatol.* **2021**, *41*, 2638–2659. [CrossRef]
4. Koster, R.D.; Suárez, M.J. Modeling the land surface boundary in climate models as a composite of independent vegetation stands. *J. Geophys. Res.* **1992**, *97*, 2697–2715. [CrossRef]
5. Doran, J.; Zhong, S. Variations in mixed-layer depths arising from inhomogeneous surface conditions. *J. Clim.* **1995**, *8*, 1965–1973. [CrossRef]
6. Lynch-Stieglitz, M. The Development and Validation of a Simple Snow Model for the GISS GCM. *J. Clim.* **1994**, *7*, 1842–1855. [CrossRef]
7. Oki, T.; Sud, Y. Design of Total Runoff Integrating Pathways (TRIP)—A global river channel network. *Earth Interact.* **1998**, *2*, 1–37. [CrossRef]
8. Kahan, D.S.; Xue, Y.; Allen, S.J. The impact of vegetation and soil parameters in simulations of surface energy and water balance in the semi-arid sahel: A case study using SEBEX and HAPEX-Sahel data. *J. Hydrol.* **2006**, *320*, 238–259. [CrossRef]
9. Guo, Z.; Dirmeyer, P.A.; Hu, Z.; Gao, X.; Zhao, M. Evaluation of the Second Global Soil Wetness Project soil moisture simulations: 2. Sensitivity to external meteorological forcing. *J. Geophys. Res. Atmos.* **2006**, *111*, D22S03. [CrossRef]
10. Veihe, A.; Quinton, J. Sensitivity analysis of EUROSEM using Monte Carlo simulation I: Hydrological, soil and vegetation parameters. *Hydrol. Process.* **2000**, *14*, 915–926. [CrossRef]
11. Dai, Y.; Yuan, H.; Xin, Q.; Wang, D.; Shangguan, W.; Zhang, S.; Liu, S.; Wei, N. Different representations of canopy structure—A large source of uncertainty in global land surface modeling. *Agric. For. Meteorol.* **2019**, *269–270*, 119–135. [CrossRef]
12. Webster, C.; Mazzotti, G.; Essery, R.; Jonas, T. Enhancing airborne LiDAR data for improved forest structure representation in shortwave transmission models. *Remote Sens. Environ.* **2020**, *249*, 15. [CrossRef]
13. Paneque-Gálvez, J.; McCall, M.K.; Napoletano, B.M.; Wich, S.A.; Koh, L.P. Small Drones for Community-Based Forest Monitoring: An Assessment of Their Feasibility and Potential in Tropical Areas. *Forests* **2014**, *5*, 1481–1507. [CrossRef]
14. Michałowska, M.; Rapiński, J. A Review of Tree Species Classification Based on Airborne LiDAR Data and Applied Classifiers. *Remote Sens.* **2021**, *13*, 353. [CrossRef]
15. Guo, Q.; Su, Y.; Hu, T.; Guan, H.; Jin, S.; Zhang, J.; Zhao, X.; Xu, K.; Wei, D.; Kelly, M.; et al. Lidar Boosts 3D Ecological Observations and Modelings: A Review and Perspective. *IEEE Geosci. Remote Sens. Mag.* **2021**, *9*, 232–257. [CrossRef]
16. Chang, M.; Zhu, S.J.; Cao, J.C.; Chen, B.Y.; Zhang, Q.; Chen, W.H.; Jia, S.G.; Krishnan, P.; Wang, X.M. Improvement and Impacts of Forest Canopy Parameters on Noah-MP Land Surface Model from UAV-Based Photogrammetry. *Remote Sens.* **2020**, *12*, 4120. [CrossRef]
17. Reutebuch, S.E.; Andersen, H.E.; McGaughey, R.J. Light detection and ranging (LIDAR): An emerging tool for multiple resource inventory. *J. For.* **2005**, *103*, 286–292. [CrossRef]

18. Korpela, I.; Ørka, H.O.; Maltamo, M.; Tokola, T.; Hyyppä, J. Tree species classification using airborne LiDAR–effects of stand and tree parameters, downsizing of training set, intensity normalization, and sensor type. *Silva Fenn* **2010**, *44*, 319–339. [CrossRef]
19. Cao, L.; Coops, N.C.; Sun, Y.; Ruan, H.; Wang, G.; Dai, J.; She, G. Estimating canopy structure and biomass in bamboo forests using airborne LiDAR data. *ISPRS J. Photogramm. Remote Sens.* **2019**, *148*, 114–129. [CrossRef]
20. Ferrarese, J.; Affleck, D.; Seielstad, C. Conifer crown profile models from terrestrial laser scanning. *Silva Fenn* **2015**, *49*, 1106. [CrossRef]
21. Guan, H.; Su, Y.; Hu, T.; Wang, R.; Ma, Q.; Yang, Q.; Sun, X.; Li, Y.; Jin, S.; Zhang, J.; et al. A Novel Framework to Automatically Fuse Multiplatform LiDAR Data in Forest Environments Based on Tree Locations. *IEEE Trans. Geosci. Remote Sens.* **2020**, *58*, 2165–2177. [CrossRef]
22. Guan, H.; Su, Y.; Sun, X.; Xu, G.; Li, W.; Ma, Q.; Wu, X.; Wu, J.; Liu, L.; Guo, Q. A marker-free method for registering multi-scan terrestrial laser scanning data in forest environments. *ISPRS J. Photogramm. Remote Sens.* **2020**, *166*, 82–94. [CrossRef]
23. Hilker, T.; Coops, N.C.; Culvenor, D.S.; Newnham, G.; Wulder, M.A.; Bater, C.W.; Siggins, A. A simple technique for co-registration of terrestrial LiDAR observations for forestry applications. *Remote Sens. Lett.* **2012**, *3*, 239–247. [CrossRef]
24. Liang, X.; Kukko, A.; Hyyppa, J.; Lehtomaki, M.; Pyorala, J.; Yu, X.; Kaartinen, H.; Jaakkola, A.; Wang, Y. In-situ measurements from mobile platforms: An emerging approach to address the old challenges associated with forest inventories. *ISPRS J. Photogramm. Remote Sens.* **2018**, *143*, 97–107. [CrossRef]
25. Pierzchala, M.; Giguere, P.; Astrup, R. Mapping forests using an unmanned ground vehicle with 3D LiDAR and graph-SLAM. *Comput. Electron. Agric.* **2018**, *145*, 217–225. [CrossRef]
26. Balsi, M.; Esposito, S.; Fallavollita, P.; Nardinocchi, C. Single-tree detection in high-density LiDAR data from UAV-based survey. *Eur. J. Remote Sens.* **2018**, *51*, 679–692. [CrossRef]
27. Guo, Q.; Su, Y.; Hu, T.; Zhao, X.; Wu, F.; Li, Y.; Liu, J.; Chen, L.; Xu, G.; Lin, G.; et al. An integrated UAV-borne lidar system for 3D habitat mapping in three forest ecosystems across China. *Int. J. Remote Sens.* **2017**, *38*, 2954–2972. [CrossRef]
28. Van der Zande, D.; Stuckens, J.; Verstraeten, W.W.; Mereu, S.; Muys, B.; Coppin, P. 3D modeling of light interception in heterogeneous forest canopies using ground-based LiDAR data. *Int. J. Appl. Earth Obs. Geoinf.* **2011**, *13*, 792–800. [CrossRef]
29. Li, W.; Guo, Q.; Tao, S.; Su, Y. VBRT: A novel voxel-based radiative transfer model for heterogeneous three-dimensional forest scenes. *Remote Sens. Environ.* **2018**, *206*, 318–335. [CrossRef]
30. Lamelas-Gracia, M.T.; Riaño, D.; Ustin, S. A LiDAR signature library simulated from 3-dimensional Discrete Anisotropic Radiative Transfer (DART) model to classify fuel types using spectral matching algorithms. *GIScience Remote Sens.* **2019**, *56*, 988–1023. [CrossRef]
31. Regaieg, O.; Yin, T.; Malenovský, Z.; Cook, B.D.; Morton, D.C.; Gastellu-Etchegorry, J.P. Assessing impacts of canopy 3D structure on chlorophyll fluorescence radiance and radiative budget of deciduous forest stands using DART. *Remote Sens. Environ.* **2021**, *265*, 112673. [CrossRef]
32. Braghiere, R.K.; Wang, Y.; Doughty, R.; Sousa, D.; Magney, T.; Widlowski, J.L.; Longo, M.; Bloom, A.A.; Worden, J.; Gentine, P.; et al. Accounting for canopy structure improves hyperspectral radiative transfer and sun-induced chlorophyll fluorescence representations in a new generation Earth System model. *Remote Sens. Environ.* **2021**, *261*, 112497. [CrossRef]
33. Wang, Y.; Köhler, P.; He, L.; Doughty, R.; Braghiere, R.K.; Wood, J.D.; Frankenberg, C. Testing stomatal models at the stand level in deciduous angiosperm and evergreen gymnosperm forests using CliMA Land (v0.1). *Geosci. Model Dev.* **2021**, *14*, 6741–6763. [CrossRef]
34. Liu, Q.; Fan, W.; Xu, B.; Zeng, Y.; Zhao, J. Regional Leaf Area Index Retrieval Based on Remote Sensing: The Role of Radiative Transfer Model Selection. *Remote Sens.* **2015**, *7*, 4604–4625. [CrossRef]
35. Puliti, S.; Talbot, B.; Astrup, R. Tree-Stump Detection, Segmentation, Classification, and Measurement Using Unmanned Aerial Vehicle (UAV) Imagery. *Forests* **2018**, *9*, 102. [CrossRef]
36. Ismail, Z.; Abdul Khanan, M.F.; Omar, F.; Abd Rahman, M.; Mohd Salleh, M.R. Evaluating Error of LiDar Derived DEM Interpolation for Vegetation Area. *Int. Arch. Photogramm. Remote. Sens. Spat. Inf. Sci.* **2016**, *XLII-4/W1*, 141–150. [CrossRef]
37. Zhou, Q.; Pilesjoe, P.; Chen, Y. Estimating surface flow paths on a digital elevation model using a triangular facet network. *Water Resour. Res.* **2011**, *47*, W07522. [CrossRef]
38. Qi, C.; Baldocchi, D.; Gong, P.; Kelly, M. Isolating individual trees in a savanna woodland using small footprint lidar data. *Photogramm. Eng. Remote Sens.* **2006**, *72*, 923–932. [CrossRef]
39. Chang, M.; Liao, W.; Wang, X.; Zhang, Q.; Chen, W.; Wu, Z.; Hu, Z. An optimal ensemble of the Noah-MP land surface model for simulating surface heat fluxes over a typical subtropical forest in South China. *Agric. For. Meteorol.* **2020**, *281*, 107815. [CrossRef]
40. Niu, G.Y.; Yang, Z.L.; Mitchell, K.E.; Chen, F.; Ek, M.B.; Barlage, M.; Kumar, A.; Manning, K.; Niyogi, D.; Rosero, E.; et al. The community Noah land surface model with multiparameterization options (Noah-MP): 1. Model description and evaluation with local-scale measurements. *J. Geophys. Res.-Atmos.* **2011**, *116*, D12109. [CrossRef]
41. Dickinson, R.E.; Shaikh, M.; Bryant, R.; Graumlich, L. Interactive Canopies for a Climate Model. *J. Clim.* **1998**, *11*, 2823–2836. [CrossRef]
42. Ball, J.T.; Woodrow, I.E.; Berry, J.A. A model predicting stomatal conductance and its contribution to the control of photosynthesis under different environmental conditions. In *Progress in Photosynthesis Research*; Springer: Berlin/Heidelberg, Germany, 1987; pp. 221–224. [CrossRef]

43. Chen, F.; Janjić, Z.; Mitchell, K. Impact of atmospheric surface-layer parameterizations in the new land-surface scheme of the NCEP mesoscale Eta model. *Bound.-Layer Meteorol.* **1997**, *85*, 391–421. [CrossRef]
44. Niu, G.; Yang, Z. Effects of vegetation canopy processes on snow surface energy and mass balances. *J. Geophys. Res. Atmos.* **2004**, *109*, D23111. [CrossRef]
45. Chen, F.; Mitchell, K.; Schaake, J.; Xue, Y.; Pan, H.; Koren, V.; Duan, Q.Y.; Ek, M.; Betts, A. Modeling of land surface evaporation by four schemes and comparison with FIFE observations. *J. Geophys. Res. Atmos.* **1996**, *101*, 7251–7268. [CrossRef]
46. Niu, G.Y.; Yang, Z.L. Effects of frozen soil on snowmelt runoff and soil water storage at a continental scale. *J. Hydrometeorol.* **2006**, *7*, 937–952. [CrossRef]
47. Barlage, M.; Tewari, M.; Chen, F.; Miguez-Macho, G.; Yang, Z.L.; Niu, G.Y. The effect of groundwater interaction in North American regional climate simulations with WRF/Noah-MP. *Clim. Chang.* **2015**, *129*, 485–498. [CrossRef]
48. Niu, G.; Yang, Z.; Dickinson, R.E.; Gulden, L.E.; Su, H. Development of a simple groundwater model for use in climate models and evaluation with Gravity Recovery and Climate Experiment data. *J. Geophys. Res. Atmos.* **2007**, *112*, D07103. [CrossRef]
49. Verseghy, D.L. CLASS—A Canadian land surface scheme for GCMs. I. Soil model. *Int. J. Climatol.* **1991**, *11*, 111–133. [CrossRef]
50. Jordan, R.E. A one-dimensional temperature model for a snow cover: Technical documentation for SNTHERM.89 *US Army Corps Eng.* **1991**, *91–16*, 49.
51. Mendoza, P.A.; Clark, M.P.; Barlage, M.; Rajagopalan, B.; Samaniego, L.; Abramowitz, G.; Gupta, H. Are we unnecessarily constraining the agility of complex process-based models? *Water Resour. Res.* **2015**, *51*, 716–728. [CrossRef]
52. Arsenault, K.R.; Nearing, G.S.; Wang, S.; Yatheendradas, S.; Peters-Lidard, C.D. Parameter Sensitivity of the Noah-MP Land Surface Model with Dynamic Vegetation. *J. Hydrometeorol.* **2018**, *19*, 815–830. [CrossRef]
53. Yinglan, A.; Wang, G.Q.; Liu, T.X.; Shrestha, S.; Xue, B.L.; Tan, Z.X. Vertical variations of soil water and its controlling factors based on the structural equation model in a semi-arid grassland. *Sci. Total Environ.* **2019**, *691*, 1016–1026. [CrossRef] [PubMed]
54. Fang, Y.; Mo, J.; Zhou, G.; Xue, J. Response of Diameter at Breast Height Increment to N Additions in Forests of Dinghushan Biosphere Reserve. *J. Trop. Subtrop. Bot.* **2005**, *13*, 198–204. [CrossRef]
55. Cheng, J.; Ouyang, X.; Huang, D.; Liu, S.; Zhang, D.; Li, Y. Sap flow characteristics of four dominant tree species in a mixed conifer-broadleaf forest in Dinghushan. *Acta Ecol. Sin.* **2015**, *35*, 4097–4104.
56. Zhang, Q.; Han, R.; Zou, F. Effects of artificial afforestation and successional stage on a lowland forest bird community in southern China. *For. Ecol. Manag.* **2011**, *261*, 1738–1749. [CrossRef]
57. Zou, S.; Geng, W.; Zhang, Q.; Zhou, G.; Liu, S.; Chu, G. A dataset of species composition in a monsoon evergreen broad- leaved forest monitoring plot of Dinghushan Forest Ecosystem Research Station (1992–2015). *China Sci. Data* **2019**, *4*, 1-7–7-7.
58. Sui, D.; Wang, Y.; Lian, J.; Zhang, J.; Hu, J.; Ouyang, X.; Fan, Z.; Cao, H.; Ye, W. Gap distribution patterns in the south subtropical evergreen broad-leaved forest of Dinghushan. *Biodiv. Sci.* **2017**, *25*, 382–392. [CrossRef]
59. Li, Y.; Mwangi, B.; Zhou, S.; Liu, S.; Zhang, Q.; Liu, J.; Chu, G.; Tang, X.; Zhang, D.; Wei, S.; et al. Effects of Typhoon Mangkhut on a Monsoon Evergreen Broad-Leaved Forest Community in Dinghushan Nature Reserve, Lower Subtropical China. *Front. Ecol. Evol.* **2021**, *9*, 692155. [CrossRef]
60. Cho, E.; Choi, M. Regional scale spatio-temporal variability of soil moisture and its relationship with meteorological factors over the Korean peninsula. *J. Hydrol.* **2014**, *516*, 317–329. [CrossRef]
61. Yang, Q.; Dan, L.; Lv, M.; Wu, J.; Li, W.; Dong, W. Quantitative assessment of the parameterization sensitivity of the Noah-MP land surface model with dynamic vegetation using ChinaFLUX data. *Agric. For. Meteorol.* **2021**, *307*, 108542. [CrossRef]
62. Chen, F.; Zhang, Y. On the coupling strength between the land surface and the atmosphere: From viewpoint of surface exchange coefficients. *Geophys. Res. Lett.* **2009**, *36*, L10404. [CrossRef]
63. Ruiz-Barradas, A.; Nigam, S. Warm season rainfall variability over the US great plains in observations, NCEP and ERA-40 reanalyses, and NCAR and NASA atmospheric model simulations. *J. Clim.* **2005**, *18*, 1808–1830. [CrossRef]
64. Garcia, M.; Saatchi, S.; Ferraz, A.; Silva, C.A.; Ustin, S.; Koltunov, A.; Balzter, H. Impact of data model and point density on aboveground forest biomass estimation from airborne LiDAR. *Carbon Balance Manag.* **2017**, *12*, 4. [CrossRef] [PubMed]
65. Chen, L.; Li, Y.; Chen, F.; Barlage, M.; Zhang, Z.; Li, Z. Using 4-km WRF CONUS simulations to assess impacts of the surface coupling strength on regional climate simulation. *Clim. Dyn.* **2019**, *53*, 6397–6416. [CrossRef]
66. White, J.C.; Wulder, M.A.; Vastaranta, M.; Coops, N.C.; Pitt, D.; Woods, M. The Utility of Image-Based Point Clouds for Forest Inventory: A Comparison with Airborne Laser Scanning. *Forests* **2013**, *4*, 518–536. [CrossRef]
67. Luo, D.; Lin, H.; Jin, Z.; Zheng, H.; Song, Y.; Feng, L.; Guo, Q. Applications of UAV digital aerial photogrammetry and LiDAR in geomorphology and land cover research. *J. Earth Environ.* **2019**, *10*, 213–226.